



2nd Advanced Optical Metrology Compendium

Advanced Optical Metrology

Geoscience | Corrosion | Particles | Additive Manufacturing: Metallurgy, Cut Analysis & Porosity



EVIDENT
OLYMPUS

WILEY

The latest eBook from **Advanced Optical Metrology**.
Download for free.

This compendium includes a collection of optical metrology papers, a repository of teaching materials, and instructions on how to publish scientific achievements.

With the aim of improving communication between fundamental research and industrial applications in the field of optical metrology we have collected and organized existing information and made it more accessible and useful for researchers and practitioners.

EVIDENT
OLYMPUS

WILEY

Rhenium Suppresses Iridium (IV) Oxide Crystallization and Enables Efficient, Stable Electrochemical Water Oxidation

Wenjing Huo, Xuemei Zhou,* Yuwei Jin, Canquan Xie, Shuo Yang, Jinjie Qian, Dong Cai, Yongjie Ge, Yongquan Qu,* Huagui Nie,* and Zhi Yang*

IrO₂ as benchmark electrocatalyst for acidic oxygen evolution reaction (OER) suffers from its low activity and poor stability. Modulating the coordination environment of IrO₂ by chemical doping is a methodology to suppress Ir dissolution and tailor adsorption behavior of active oxygen intermediates on interfacial Ir sites. Herein, the Re-doped IrO₂ with low crystallinity is rationally designed as highly active and robust electrocatalysts for acidic OER. Theoretical calculations suggest that the similar ionic sizes of Ir and Re impart large spontaneous substitution energy and successfully incorporate Re into the IrO₂ lattice. Re-doped IrO₂ exhibits a much larger migration energy from IrO₂ surface (0.96 eV) than other dopants (Ni, Cu, and Zn), indicating strong confinement of Re within the IrO₂ lattice for suppressing Ir dissolution. The optimal catalysts (Re: 10 at%) exhibit a low overpotential of 255 mV at 10 mA cm⁻² and a high stability of 170 h for acidic OER. The comprehensive mechanism investigations demonstrate that the unique structural arrangement of the Ir active sites with Re-dopant imparts high performance of catalysts by minimizing Ir dissolution, facilitating *OH adsorption and *OOH deprotonation, and lowering kinetic barrier during OER. This study provides a methodology for designing highly-performed catalysts for energy conversion.

1. Introduction

The unsatisfactory activity and stability of electrocatalysts for the oxygen evolution reaction (OER) restricts the performance of many electrochemical devices—such as electrolyzers, rechargeable metal–air batteries, and regenerative fuel cells.^[1–3]

W. Huo, X. Zhou, Y. Jin, C. Xie, J. Qian, D. Cai, Y. Ge, H. Nie, Z. Yang
Key Laboratory of Carbon Materials of Zhejiang Province
Wenzhou University
Wenzhou 325035, P. R. China
E-mail: zxm.mei@163.com; huaguinie@126.com; yang201079@126.com

S. Yang
College of Electrical and Electronic Engineering
Wenzhou University
Wenzhou 325035, P. R. China

Y. Qu
Key Laboratory of Special Functional and Smart Polymer Materials of
Ministry of Industry and Information Technology
School of Chemistry and Chemical Engineering
Northwestern Polytechnical University
Xi'an 710072, P. R. China
E-mail: yongquan@nwpu.edu.cn

 The ORCID identification number(s) for the author(s) of this article can be found under <https://doi.org/10.1002/smll.202207847>.

DOI: 10.1002/smll.202207847

Such a four-electron transfer reaction involving multiple reaction intermediates exhibits sluggish OER kinetics, leading to substantial overpotentials and losses in energy efficiency.^[4–7] To date, noble metal oxides (such as IrO₂ or RuO₂) afford the most satisfactory activity among various OER electrocatalysts.^[8–10] In particular, improved intrinsic OER activities of Ir-based catalysts have been proposed by various strategies including alloying,^[11–13] formation of hybrids with other metal oxides,^[14] amorphous or low-crystalline characteristics,^[15] and participation of lattice oxygen.^[16] However, their high OER activities usually accompany with low stability. These materials generally readily degrade because of structural aggregation and collapse of nanostructured active species, as well as dissolution of active sites.^[17,18] Therefore, developing a novel strategy to afford high catalytic activity as well as robust stability of Ir-based OER electrocatalysts is highly desired.

Anchoring nanostructured active species on a supported surface is a common strategy for minimizing aggregation.^[19,20] However, many supports also exhibit substantial stability issues under high overpotentials and strong acidic conditions. Furthermore, dissolution of Ir is related with the coordination environment because the latter determines the interactions between Ir and water.^[17] Doping is facile and straightforward with regard to tuning the coordination environment, and thus improves electrocatalytic OER performance.^[21] Recently, it was reported that hollow M-doped IrCu octahedral nanocrystals (M = Co, Mn, or Zn) exhibited superior OER stability, owing to the unique structure arrangement with a strong interconnection of the [IrO₆] octahedral.^[22,23] Compared with the bare IrO₂ without dopants, theoretical calculations indicated that doping W into the IrO₂ lattice induced stronger hybridization between the Ir 5d and O 2p orbitals, and hence minimized the dissolution of Ir.^[24] However, excessively strong hybridization between the transition metal d and O 2p orbitals might result in surface amorphization or even structural collapse during the OER.^[17] Thus, a dopant with high electrochemical stability, multiple valence states, and tailorable oxygen capacity are highly demanded, providing a potential solution for solving the activity as well as stability issues of Ir-based electrocatalysts for the acidic OER.

Recently, rhenium oxides has been utilized as one of the most promising electrocatalysts in the electrochemical field because of its high electrical conductivity and reversible ion movements,^[25–27] which originates from the substantial broadening of the 5d conduction band by the hybridization between the Re 5d and O 2p atomic orbitals.^[28] Because of their similar ionic radii (≈ 0.063 nm), the original structure of IrO₂ would be maintained after introducing Re into the crystal lattice of IrO₂. More importantly, the multiple valence states and adjustable oxygen capacity of Re enables the modulation of the unique structural arrangement of IrO₂, probably resulting in the mitigation of Ir dissolution. Additionally, chemical doping by Re increases the recrystallization temperature, consequently suppressing the crystallinity of IrO₂ and thereby improving the OER activity.^[29] Considering the aforementioned facts, Re-doped IrO₂ is expected to realize both high catalytic activity and robust stability for the acidic OER.

2. Result and Discussion

2.1. The Substitution Energy and Migration Energy of Re–IrO₂ by DFT Calculations

Initially, density function theory (DFT) calculations were performed to analyze the electronic and geometrical structures of IrO₂ with Re-doped IrO₂ (Figure 1). DFT calculations indicate a negative substitution energy, suggesting favorable chemical doping of Re into the crystal lattice of IrO₂. To further investigate this phenomenon, Ni (0.069 nm, 1.9), Cu (0.073 nm, 1.9), and Zn (0.074 nm, 1.6)—all of which exhibit a similar ionic radius and electronegativity (as listed parenthetically in the previous text) compared with Re—were introduced into the IrO₂ structure (Figure S1 and Table S1, Supporting Information). The Re substitutional energies (−1.62 eV) were lower than corresponding values of Ni (1.54 eV), Cu (3.92 eV), and Zn (3.94 eV); indicating that Re-doping into IrO₂ was the most

straightforward among the various dopants (Figure 1c and Table S1, Supporting Information). Additionally, Re-doped IrO₂ exhibited the largest migration energy from the IrO₂ surface (0.96 eV) in comparison with the other dopants, indicating that the Re dopants were strongly confined within the IrO₂ lattice and the catalyst surface. These results indicate that Re-doped IrO₂ might strongly disrupt the IrO₂ matrix and modulate the crystallinity as well as the surface physicochemical properties, and thereby improve the activity as well as the stability of the electrocatalyst for the OER.

2.2. The Preparation and Characterization of Re–IrO₂

Re-doped IrO₂ electrocatalysts with various doping levels were synthesized by a facile sol–gel approach followed by calcination at temperatures of 300, 330, 350, 450, and 700 °C. As indicated by the powder X-ray diffraction (XRD) patterns of Re-doped IrO₂ at a doping level of 10 at% (Re_{0.1}–IrO₂, Figure S2, Supporting Information), two characteristic peaks of 28° and 34° were ascribed to (110) and (101) of the rutile phase IrO₂, respectively. With increasing treatment temperature, the crystallinity of the as-grown electrocatalysts became increasingly evident. The low-crystallinity of Re_{0.1}–IrO₂ was identified as 330 °C. To evaluate the influence of various dopant elements and temperatures on the crystallinity, Ni_{0.1}–IrO₂, Cu_{0.1}–IrO₂, and Zn_{0.1}–IrO₂ electrocatalysts were also prepared under the same conditions at 330 °C. The Re-doped electrocatalysts exhibited the lowest crystallinity among all the as-synthesized electrocatalysts (Figure 2a), indicating that the IrO₂ crystallization could be minimized after introducing Re under the same synthetic protocol in comparison with Ni, Cu, and Zn dopants; in agreement with DFT calculations. In addition, as observed from the thermogravimetric (TG) and differential thermogravimetric (DTG) curves (Figure S3, Supporting Information), the decomposition temperature of Re_{0.1}–IrO₂ (400 °C) was higher than that of IrO₂ (345 °C), which imparted high heat resistance and affected the IrO₂ crystallization. Furthermore, the intensities of the characterized Raman peaks of Re_{0.1}–IrO₂ at 558 and 719 cm^{−1} were lower than those of Ni_{0.1}–IrO₂, Cu_{0.1}–IrO₂, and Zn_{0.1}–IrO₂, again indicating the low crystallization of Re_{0.1}–IrO₂ (Figure 2b). Additionally, the location of Raman peaks of Re_{0.1}–IrO₂ were also the same as those of IrO₂ and no Raman peaks of Re oxygen compounds were observed, demonstrating chemical doping of Re into the lattice of IrO₂ instead of formation of ReO_x phases.^[30] These theoretical analyses and experimental results strongly indicated that Re was doped into IrO₂ and the introduction of Re could minimize the crystallization of IrO₂, due to the spontaneous substitution energy and high sintering resistance.

Typical transmission electron microscopy (TEM) images of Re_{0.1}–IrO₂ (Figure 2c and Figure S4, Supporting Information) indicated that the Re_{0.1}–IrO₂ electrocatalysts were in the form of nanoparticles with an average size of 2.65 nm. The measured interplanar spacing of 0.226 nm was assigned to the (200) facets of rutile IrO₂ (Figure 2d), in agreement with the XRD patterns. The average crystallite sizes and crystallinity of as-grown electrocatalysts at various temperatures as well as various Re doping levels were further investigated with the

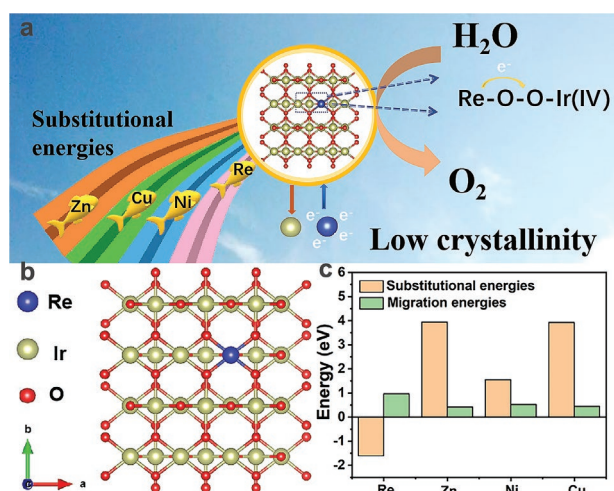


Figure 1. a) Schematic diagram of the rationally designed electrocatalysts; b) structure of Re–IrO₂ derived from DFT calculations; c) substitutional energies and migration energies of IrO₂ doped with different elements (Re, Zn, Ni, and Cu).

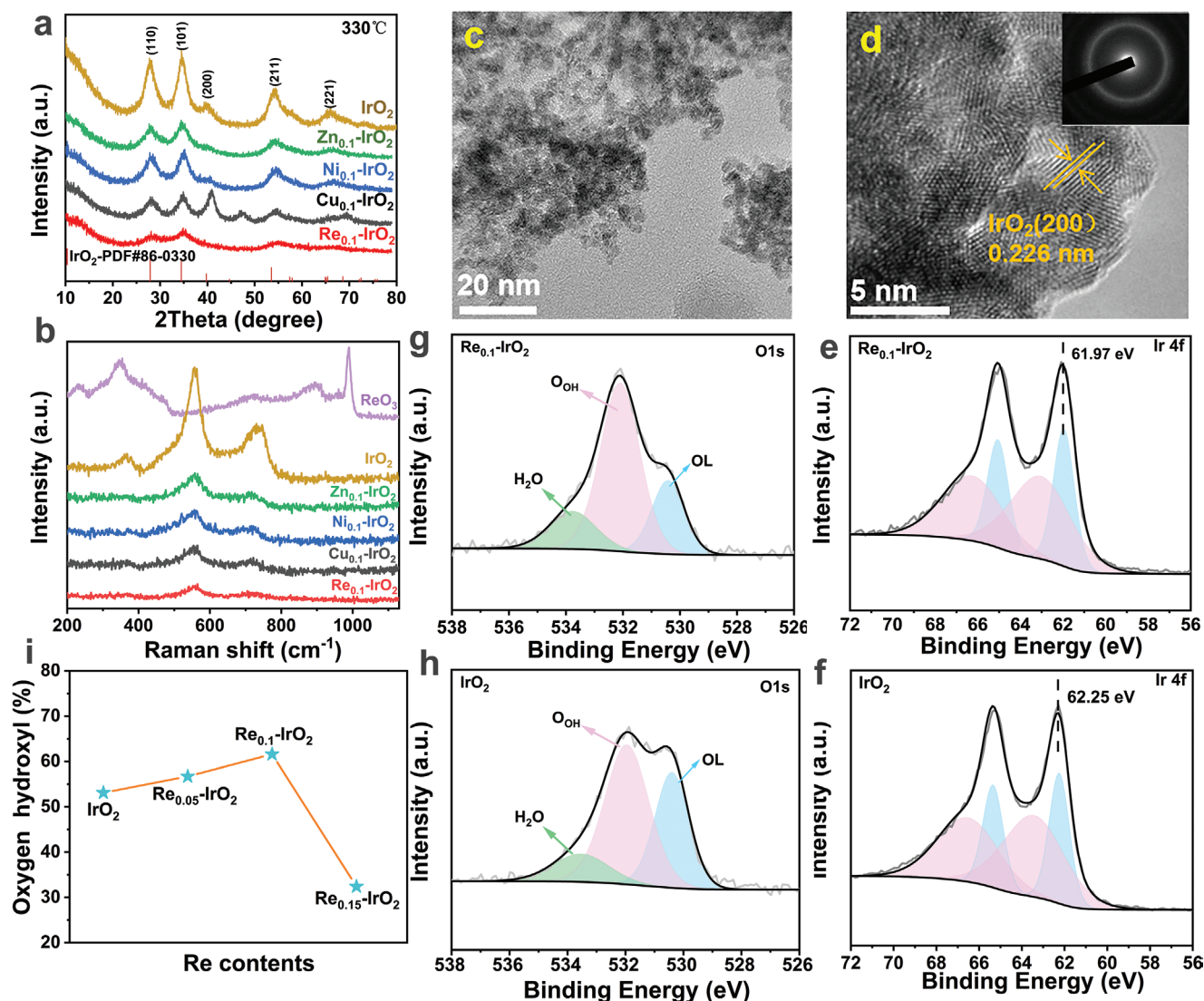


Figure 2. Characterization of as-obtained products. a) XRD and b) Raman patterns of $\text{Zn}_{0.1}\text{-IrO}_2$, $\text{Ni}_{0.1}\text{-IrO}_2$, $\text{Cu}_{0.1}\text{-IrO}_2$, $\text{Re}_{0.1}\text{-IrO}_2$, IrO_2 ; c) TEM images, d) high-resolution TEM images of $\text{Re}_{0.1}\text{-IrO}_2$ calcined at $330\text{ }^\circ\text{C}$; XPS spectra of Ir 4f of e) $\text{Re}_{0.1}\text{-IrO}_2$ and f) IrO_2 ; XPS spectra of O 1s of g) $\text{Re}_{0.1}\text{-IrO}_2$ and h) IrO_2 ; i) relationship between oxygen hydroxyl and Re contents.

Scherrer's equation based on the XRD peaks. The average crystallite size and crystallinity increased with increasing annealing temperature under the same doping level of Re (Figure S5, Supporting Information). A similar tendency was also observed for samples with increasing doping levels of Re under the same annealing temperature (Figure S6, Supporting Information). $\text{Re}_{0.15}\text{-IrO}_2$ that was calcinated at $330\text{ }^\circ\text{C}$ exhibited the lowest crystallinity and smallest particle size (Figures S5 and S6, Supporting Information). However, the newly evident Raman peaks of $\text{Re}_{0.15}\text{-IrO}_2$ at 912 and 967 cm^{-1} could be attributed to Re–O (Figure S7, Supporting Information),^[30] suggesting that the high Re-doping level in IrO_2 (>15 at%) resulted in the precipitation of ReO_x phase. Additionally, the real ratios of Ir and Re were applied to characterize by inductively coupled plasma-mass spectrometry (ICP-MS), as given in Table S2, Supporting Information, which were closely related to the addition of the amounts of precursors.

Next, X-ray photoelectron spectroscopy (XPS) measurements were carried out to evaluate the influence of the incorporated Re dopant on the electronic structure of IrO_2 . Consistent with elemental mapping images (Figure S8, Supporting Information), the XPS profiles further confirmed that all of the Re– IrO_2 electrocatalysts consisted of Re, Ir, and O (Figure S9, Supporting Information). High-resolution Ir 4f profiles indicated that there were four Ir 4f peaks: including $\text{Ir}^{4+}4f_{7/2}$ (62.25 eV), $\text{Ir}^{4+}4f_{5/2}$ (65.37 eV), $\text{Ir}^{3+}4f_{5/2}$ (63.56 eV), and $\text{Ir}^{3+}4f_{7/2}$ (65.48 eV),^[31] as given in Figure 2e and Figure S10, Supporting Information. Notably, the binding energies of $\text{Ir}4f_{7/2}$ and $\text{Ir}4f_{5/2}$ in $\text{Re}_{0.05}\text{-IrO}_2$ and $\text{Re}_{0.1}\text{-IrO}_2$ decreased in comparison with IrO_2 . In contrast, the binding energy of Re 4f increased to higher binding energies (Figure S11, Supporting Information). Such electronic structural evolutions of various electrocatalysts indicate strong electronic modulation after introducing Re into pristine IrO_2 . Furthermore, the high-resolution profiles of O 1s

were deconvoluted into three peaks: corresponding to surface lattice oxygen (O_L , 530.4 eV), coordinatively unsaturated oxygen or oxygen in the hydroxyl group (O_{OH} , 531.9 eV), and adsorbed H_2O , respectively (533.5 eV) (Figure 2g,f and Figure S12, Supporting Information).^[32,33] The percentage of O_{OH} in $Re_{0.1}-IrO_2$ was higher than those in other electrocatalysts, which influenced the Ir–O correlations (Figure 2i and Table S3, Supporting Information).

2.3. OER Activity of As-Grown Catalysts

The previously discussed theoretical and experimental results indicate that substitution of Re into IrO_2 can reduce the crystallinity of IrO_2 , increasing the number of surface O_{OH} species and modulating the local electronic structure of IrO_2 as well as the surrounding environment of the active sites. Accordingly, this substitution potentially affects the OER performance. Thus, the OER performance of the as-obtained electrocatalysts was evaluated with a three-electrode system in 0.5 M H_2SO_4 . A graphite rod and saturated calomel electrode (SCE) were employed as the counter and reference electrodes, respectively. All of the electrocatalysts were uniformly coated on carbon fiber paper at a mass loading of 0.56 mg cm^{-2} . The activities of various catalysts for OER were typically characterized by linear scan voltammetry (LSV) with 90% iR correction. The $Re_{0.1}-IrO_2$ electrocatalysts exhibited higher electrocatalytic activities than those of other electrocatalysts with different Re-doping levels ($Re_{0.05}-IrO_2$, $Re_{0.15}-IrO_2$) under each calcination temperature (330, 350, 450, and 700 °C) over the entire potential range (Figure 3a and Figure S13, Supporting Information). Furthermore, the $Re_{0.1}-IrO_2$ catalyst that was calcinated at 330 °C exhibited the highest OER activity among the three catalysts (Figure 3b). The derived overpotential of $Re_{0.1}-IrO_2$ at 330 °C (255 mV) was lower than that of $Re_{0.05}-IrO_2$ (268 mV), $Re_{0.15}-IrO_2$ (290 mV), IrO_2 (312 mV), and commercial IrO_2 (denoted as C- IrO_2 , 338 mV) at 10 mA cm^{-2} . The enhanced catalytic activity of $Re_{0.1}-IrO_2$ was also indicated by the lowest Tafel slope of 65.6 mV dec^{-1} ; which was smaller than those of $Re_{0.05}-IrO_2$, $Re_{0.15}-IrO_2$, IrO_2 , and C- IrO_2 (Figure 3c). These values indicated that $Re_{0.1}-IrO_2$ treated at 330 °C enabled straightforward adsorption of water and enhanced reaction kinetics, because of the comparatively lower crystallinity and abundant surface O_{OH} species of the electrocatalysts upon introduction of Re (Figure 2g). However, $Re_{0.15}-IrO_2$ treated at 330 °C (with the lowest crystallinity and smallest particle size) exhibited unsatisfactory OER activity, which could be attributed to the low number of surface O_{OH} species that corresponds to phase separation and formation of ReO_x (Figure 2g).

Next, to investigate the influence of various dopants, the OER catalytic activities of $Ni_{0.1}-IrO_2$, $Cu_{0.1}-IrO_2$, and $Zn_{0.1}-IrO_2$ calcinated at 330 °C were also measured under the same conditions (Figure S14, Supporting Information). These results also indicated that $Re_{0.1}-IrO_2$ treated at 330 °C exhibited a higher electrocatalytic activity than that of $Ni_{0.1}-IrO_2$ (325 mV), $Cu_{0.1}-IrO_2$ (314 mV), and $Zn_{0.1}-IrO_2$ (286 mV) at a current density of 10 mA cm^{-2} . The overpotential of the $Re_{0.1}-IrO_2$ catalyst at a specific current density of 10 mA cm^{-2} was comparable with or even superior to the majority of the reported Ir-based electrocatalysts (Table S4, Supporting Information). All of the previously

discussed phenomena indicated that the $Re_{0.1}-IrO_2$ electrocatalysts exhibited excellent OER activities, facilitated by the advantages of low crystallization and high percentage of O_{OH} .

2.4. Revealing the Origin of OER Activity by the Electrochemical Measurements

The improved OER activities of IrO_2 after chemical doping by Re were systematically examined by various electrochemical characterizations. First, electrochemical impedance spectroscopy (EIS) was employed to evaluate charge transfer. The Nyquist plots (Figure S15, Supporting Information) of the EIS data at open circuit voltage for the $Re_{0.1}-IrO_2$ electrode indicated a semicircle associated with the smallest charge transfer resistance and the largest Warburg resistance among all of the catalytic electrodes, indicating the most rapid electron transfer and the most efficient chemical diffusion within the $Re_{0.1}-IrO_2$ electrode. This result could be attributed to the modulated electronic structure of IrO_2 by incorporation of Re. Next, the electrochemically active surface area (ECSA) was calculated from the electrochemical double-layer capacitance (C_{dl}) based on cyclic voltammetry (CV) (Figure S16, Supporting Information).^[34] The slope of the corresponding linear fitting of $Re_{0.1}-IrO_2$ was larger than that of the other electrodes (Figure 3d and Table S5, Supporting Information), indicating that the $Re_{0.1}-IrO_2$ electrode exhibited a large number of active sites and a large electrochemically active surface area. Additionally, the Brunauer–Emmett–Teller surface area of $Re_{0.1}-IrO_2$ (135.5 $m^2 g^{-1}$) was larger than that of $Re_{0.05}-IrO_2$ (106.7 $m^2 g^{-1}$), $Re_{0.15}-IrO_2$ (124.1 $m^2 g^{-1}$), and IrO_2 (108.8 $m^2 g^{-1}$) (Figure S17, Supporting Information); indicating that $Re_{0.1}-IrO_2$ exhibited the largest surface area and the largest number of active sites, and thereby improved the OER activity.

An appropriate affinity adsorption energy of oxygenated intermediates at the surface active sites plays an important role in the catalytic activity during the OER.^[35,36] The adsorption affinity of intermediates (OH^* , O^* , and OOH^*) on the active sites of $Re_{0.1}-IrO_2$ and IrO_2 were carried out with methanol as a probe molecule to detect oxygen intermediates through their electrophilicity.^[37] Figure 3e,f, and Figure S18, Supporting Information, indicate the differences in the LSV curves in the absence and presence of methanol for IrO_2 , $Re_{0.05}-IrO_2$, $Re_{0.1}-IrO_2$, and $Re_{0.15}-IrO_2$. The surface coverage of OH^* varied in a trend of $IrO_2 > Re_{0.1}-IrO_2 > Re_{0.15}-IrO_2 > Re_{0.05}-IrO_2$; indicating that the optimal binding energy of OH^* and O^* on $Re_{0.1}-IrO_2$ was neither too strong nor too weak. The adsorption of intermediates was further confirmed by DFT calculations (Figure S19, Supporting Information). The d-band center relative to the Fermi level of IrO_2 was -4.2 eV. Regarding $Re_{0.1}-IrO_2$, the d-band center was -3.4 eV versus the Fermi level. The modulations of the d orbitals of Ir (which correspond to the involved Re atoms) could optimize the binding strength of O^* and HOO^* intermediates on the catalyst surface, and thereby facilitate charge transfer as well as enhance the OER kinetics in a manner that imparts high OER activity.^[38]

To obtain in-depth understanding of the catalytic kinetics, adsorption of oxygenated intermediates on the surface of the $Re_{0.1}-IrO_2$ electrode during the OER was further investigated by operando EIS measurements.^[39] Figure 3g,h shows

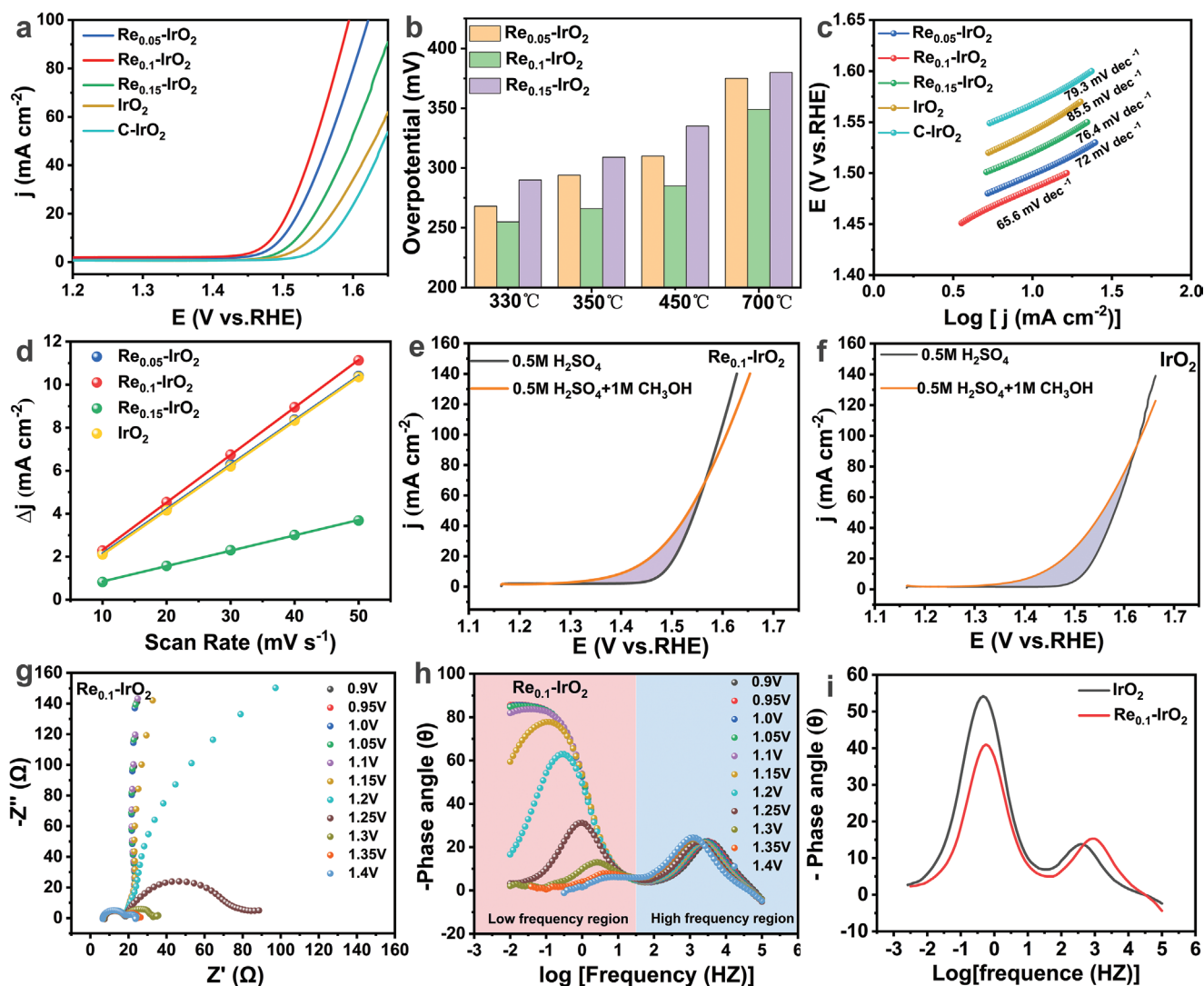


Figure 3. OER activity of the Re-IrO₂ catalyst. a) LSV for Re-IrO₂ prepared at 330 °C with different Re contents in 0.5 M H₂SO₄; b) the relationship between overpotential and the catalysts with the different temperature at the current density of 10 mA cm⁻²; c) Tafel plots calculated from (a); d) charging current density differences plotted versus scan rate; e) Re_{0.1}-IrO₂ and f) IrO₂ in 0.5 M H₂SO₄ in the presence or absence of methanol (1.0 M) solution; g) Nyquist plots and h) bode phase plots for Re_{0.1}-IrO₂ catalysts at different applied potentials versus SCE in 0.5 M H₂SO₄; i) bode phase plots of pure IrO₂ and Re_{0.1}-IrO₂ at 1.3 V versus SCE.

typical Nyquist plots as well as bode phase plots of Re_{0.1}-IrO₂ over a potential range of 0.9–1.4 V (vs SCE), where IrO₂ was also measured as the control catalyst (Figure S20, Supporting Information). An equivalent circuit was employed to fit these Nyquist plots at various applied potentials (Figure S21, Supporting Information). The variation of the charge transfer resistance (R_{ct}) and constant-phase element (CPE_{ct}) can indicate the *OH evolution on the catalyst surface.^[30] Because Re_{0.1}-IrO₂ and IrO₂ exhibited similar solution resistances (R_s), the variation of the total resistance (R_{total}) was determined by R_{ct} . The calculated R_{ct} and CPE_{ct} of Re_{0.1}-IrO₂ were lower than corresponding values of IrO₂ at a given applied potential (such as 1.3 V vs SCE, Table S6, Supporting Information), indicating much faster kinetics in terms of adsorbed *OH for the Re_{0.1}-IrO₂ electrode during the OER. Figure 3i shows a bode phase plot of Re_{0.1}-IrO₂ and IrO₂ at 1.3 V (vs SCE). The impedance

response within the lower-frequency region could correspond to the OER over the metal oxyhydroxide, which confirmed that the evolved metal oxyhydroxide phase was responsible for the OER catalytic centers. Compared with IrO₂, the phase peak of Re_{0.1}-IrO₂ at the low-frequency interface exhibited a lower phase angle, which could be attributed to faster deprotonation of *OOH intermediates.^[35,36] These results confirm the positive effects of the Re dopants on the overall reaction kinetics including rapid adsorption of *OH and deprotonation of *OOH intermediates during the electron transfer steps of the OER.

2.5. Understanding the OER Mechanism by DFT Calculations

To further reveal the OER mechanism, DFT calculations were performed on the basis of three models: including ideal rutile

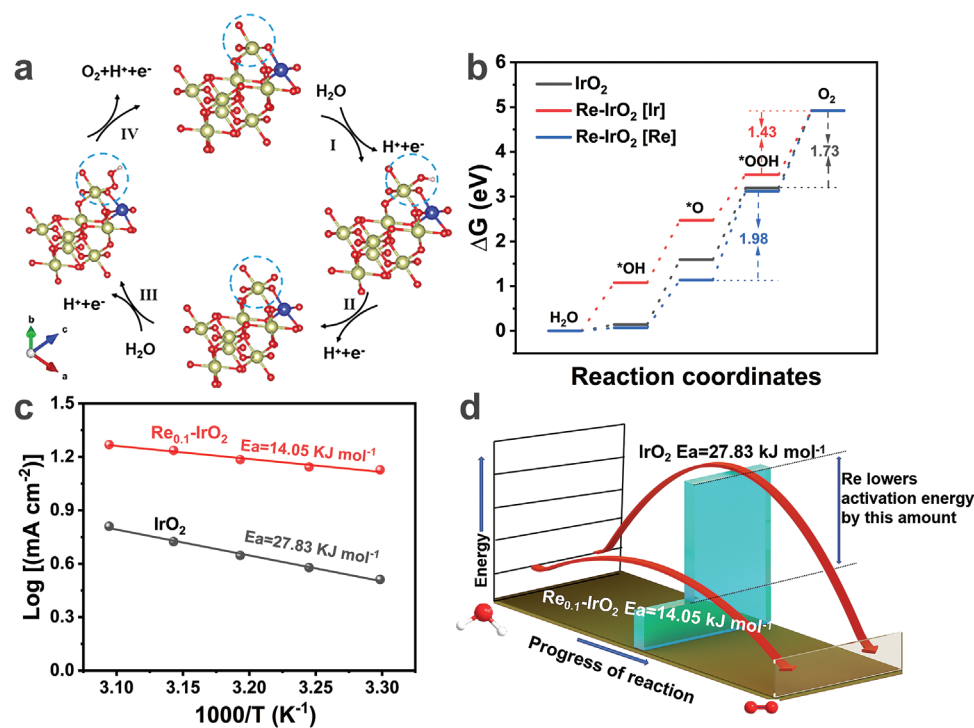


Figure 4. a) The four electron OER pathway of Re-IrO₂; b) computed overpotential versus different catalysts. c,d) Arrhenius plots of the kinetic currents illustration of different activation energy of OER at 1.5 V versus RHE for Re_{0.1}-IrO₂ and IrO₂.

IrO₂, Re-IrO₂[Ir] (Ir acting as active sites), and Re-IrO₂[Re] (Re acting as active sites) (Figure 4a; Figures S22 and S23, Supporting Information). The Supporting Information shows all of the calculative details for DFT calculations. Based on previous investigations, the adsorption energies of oxygen-based intermediates (*OH, *O, and *OOH) closely correspond to the OER activities.^[32,40] Figure 4b shows the energy barriers of all of the reaction intermediates (such as *OH, *O, and *OOH) in the OER. Regarding Re-IrO₂[Re], the rate-determining step (RDS) from *O to *OOH exhibited a higher energy barrier of 1.98 eV in comparison with those of Re-IrO₂[Ir] and IrO₂, indicating that Re was not the catalytic active site. Regarding pristine IrO₂, the RDS from OOH* to O₂ exhibited an energy barrier of 1.73 eV. After introducing Re, the electronic configuration of IrO₂ was redistributed; thus, conversion of OOH* into O₂ for Re-IrO₂[Ir] exhibited a much lower overpotential of 1.43 eV in comparison with IrO₂ (1.73 eV). This result suggests a lower OOH* adsorption energy at the Ir site in the model of Re-IrO₂[Ir] and thereby a higher OER activity. These results were further confirmed by the apparent activation energy (E_a). A temperature-dependent kinetic analysis of both Re_{0.1}-IrO₂ and IrO₂ electrodes was conducted to extract the E_a of the two catalysts for the acidic OER.^[41,42] LSV curves of Re_{0.1}-IrO₂ and IrO₂ electrodes were recorded in 0.5 M H₂SO₄ over a temperature range of 303.15 to 323.15 K (Figure S24, Supporting Information). As expected, the catalytic activities of both electrodes increased with increasing temperature. The E_a values of both catalysts at 1.5 V (vs reversible hydrogen electrode [RHE]) were calculated through the Arrhenius equation (Figure 4c). The derived value of E_a for Re_{0.1}-IrO₂ was 14.05 kJ mol⁻¹, much lower than that of

IrO₂ (27.83 kJ mol⁻¹), indicating a much lower kinetic barrier for the OER upon introduction of Re into IrO₂ (Figure 4d) and thus improved OER performance.

2.6. Revealing the Origin of OER stability of Re-IrO₂

Additionally, the stability in acidic media is a particularly important parameter for evaluating electrocatalysts in the field of practical application. The stability test of Re_{0.1}-IrO₂, Cu_{0.1}-IrO₂, Zn_{0.1}-IrO₂, Ni_{0.1}-IrO₂, and C-IrO₂ in acidic media was determined by chronopotentiometry at the current density of 10 mA cm⁻², as shown in Figure 5a. The stability of doped-IrO₂ was all longer than that of C-IrO₂ (around 40 h), suggesting that chemical doping could adjust the structure of IrO₂ to mitigate of Ir dissolution. Furthermore, Re_{0.1}-IrO₂ was extremely stable at 10 mA cm⁻² for nearly 170 h, compared that of Ni_{0.1}-IrO₂ (110 h), Cu_{0.1}-IrO₂ (90 h), and Zn_{0.1}-IrO₂ (90 h). Interestingly, the stability order was consistent with the migration energy from the IrO₂ surface (Re_{0.1}-IrO₂ (0.96 eV) > Ni_{0.1}-IrO₂ (0.52 eV) > Cu_{0.1}-IrO₂ (0.44 eV) > Zn_{0.1}-IrO₂ (0.41 eV)) based on DFT calculations (Table S1, Supporting Information). A multi-step chronopotentiometric curve for the Re_{0.1}-IrO₂ electrode was recorded by varying the catalytic current densities from 10, 20, and 30 mA cm⁻² (Figure S25, Supporting Information). The potential of the Re_{0.1}-IrO₂ electrode at 10 mA cm⁻² completely reverted back to the initial values obtained at 10 mA cm⁻² after measurements at various current densities, which implied mechanical robustness of the Re_{0.1}-IrO₂ electrode. Additionally, the element mapping results of Re_{0.1}-IrO₂ after the stability test

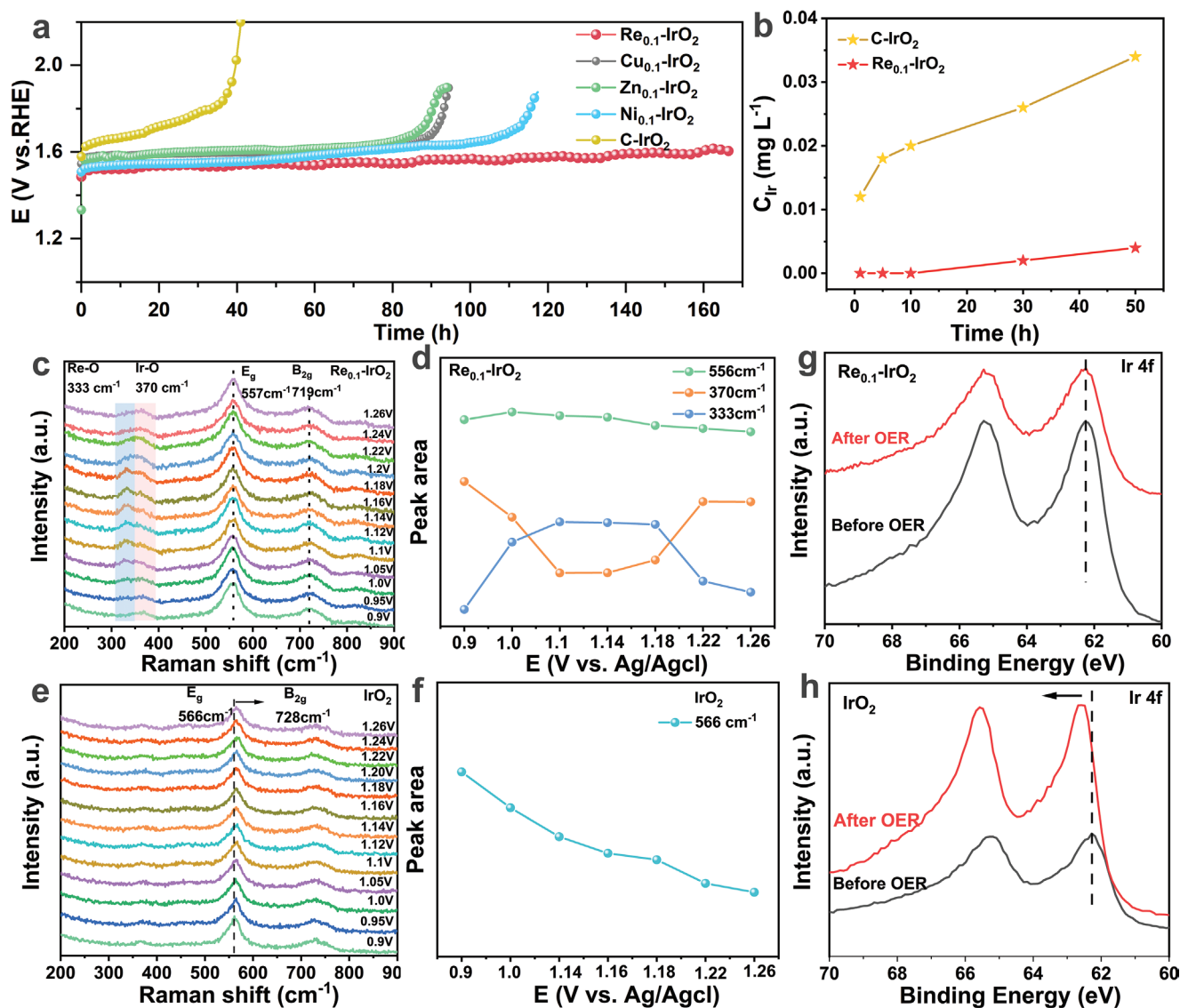


Figure 5. a) Long-term electrochemical stability of $\text{Re}_{0.1}\text{-IrO}_2$ and C-IrO_2 was measured at the current density of 10 mAcm^{-2} . b) ICP-MS results of $\text{Re}_{0.1}\text{-IrO}_2$ and IrO_2 ; in situ Raman spectra of c) $\text{Re}_{0.1}\text{-IrO}_2$ and e) IrO_2 during the OER process; Peak area variations were taken from in situ Raman of d) $\text{Re}_{0.1}\text{-IrO}_2$ and f) IrO_2 ; ex situ Ir 4f XPS spectra of g) $\text{Re}_{0.1}\text{-IrO}_2$ and h) IrO_2 .

are presented in Figure S26, Supporting Information. These results indicated strong confinement of Re within the IrO_2 lattice for suppressing Ir dissolution, analogous to the majority of the reported Ir-based catalysts with high OER performance in acidic electrolytes (Table S4, Supporting Information).

In addition, S-number served as a baseline metric of stability and was calculated by the ratio between the amount of evolved O_2 at an estimated 100% faradaic efficiency and the amount of dissolved active metal (the details in the Supporting Information).^[34,43,44] In turn, the dissolved Ir concentration ($[\text{Ir}]$ in mg L^{-1}) of the $\text{Re}_{0.1}\text{-IrO}_2$ and IrO_2 electrocatalysts was examined by ICP-MS during long-term testing at high potential under strongly acidic conditions (Figure 5b), and the amount of dissolved Ir that occupied the total catalyst loadings on the electrode was calculated and summarized in Table S7, Supporting Information. The negligibly dissolved Ir was observed

for $\text{Re}_{0.1}\text{-IrO}_2$ during the initial 10 h; whereas a substantial quantity of Ir was dissolved for IrO_2 under the same operations (Figure 5b and Table S7, Supporting Information). By comparing the Ir dissolution of the two catalysts at intervals, the much lower Ir dissolution rate ($8.6 \times 10^{-5} \text{ mg L}^{-1} \text{ h}^{-1}$) of the $\text{Re}_{0.1}\text{-IrO}_2$ electrode indicates its excellent electrochemical stability during operation, which could be attributed to the higher corrosion resistance. Furthermore, S-number values were calculated in Table S8, Supporting Information. The higher the number stands for the more stable of the electrocatalyst.^[44] The S-number values of $\text{Re}_{0.1}\text{-IrO}_2$ were 3.7×10^{10} (30 h) and 3.1×10^{10} (50 h), which was higher than those of IrO_2 (2.8×10^9 at 30 h; 3.6×10^9 at 50 h) during constant current measurements. These results indicated that $\text{Re}_{0.1}\text{-IrO}_2$ electrocatalysts exhibited long-time stability, which is strongly correlated to the contribution of Re.

Next, to understand the roles of Re dopants in the modulated electronic states of Ir and the substantially increased catalytic stability of $\text{Re}_{0.1}\text{-IrO}_2$ for the acidic OER, in situ Raman spectroscopy (a sensitive probe for detecting the surface structure of catalysts) was performed.^[45] Before applying the external potential, typical Raman peaks of $\text{Re}_{0.1}\text{-IrO}_2$ at 370, 557, and 726 cm^{-1} were identified as Ir–O as well as the E_g and B_{2g} vibrational modes of the IrO_6 octahedra in IrO_2 (Figure 5c).^[45] With increasing applied potential, a new Raman peak at 333 cm^{-1} was evident, which was assigned to Re–O.^[30] Before the OER, the intensity of the Re–O peak increased, whereas that of Ir–O at 370 cm^{-1} decreased. When the external potentials were sufficiently high to enhance the OER, this Re–O peak was no longer evident; whereas the Ir–O Raman peak at 370 cm^{-1} was retained (Figure 5d). Furthermore, the intensity of the 557 cm^{-1} peak was almost unchanged. As a comparison, the intensity of the Raman peak (566 cm^{-1}) of the IrO_2 electrocatalysts decreased with increasing potential during the OER (Figure 5e,f), indicating the dissolution caused by forming the high valence state of Ir. As indicated by a comparison of the Raman spectra of the two catalysts, the manifestation/elimination of the Re–O Raman peak at 333 cm^{-1} and the well-preserved Ir–O Raman peaks of $\text{Re}_{0.1}\text{-IrO}_2$ during catalysis strongly suggest suppressed over-oxidation of Ir, which was modulated by Re dopants with multiple valence states and a large migration energy from IrO_2 , in accord with DFT analysis. Consequently, electrochemical dissolution of Ir was substantially mitigated in $\text{Re}_{0.1}\text{-IrO}_2$, in agreement with the ICP results.

To examine the oxidation states of Ir in the spent $\text{Re}_{0.1}\text{-IrO}_2$ and IrO_2 electrocatalysts, ex situ XPS measurements were performed (Figure 5g,h). After the OER, the shift of the XPS peak of IrO_2 toward higher binding energy indicates the formation of surface iridium species in a higher valence state, which is also one of the important reasons for the IrO_2 instability. In contrast, the XPS peaks of Re 4f in the Re-doped IrO_2 catalysts gradually shifted to higher binding energies with increasing applied potential (Figure S27, Supporting Information), whereas the binding energies of the Ir 4f XPS peaks in the $\text{Re}_{0.1}\text{-IrO}_2$ electrode were negligibly affected (Figure 5f), thus indicating the enhanced OER stability. The XPS profiles of the two catalysts are highly consistent with the in situ Raman measurements, demonstrating the roles of the Re dopant in suppressing the over-oxidation of Ir during the OER and enhancing the catalytic stability afterward.

Additionally, in situ attenuated total reflection infrared (ATR-IR) spectro-electrochemical measurements were carried out to detect the OOH intermediate. The recorded peak at $\approx 1157 \text{ cm}^{-1}$ was assigned to the characteristic vibration adsorption of the surface-adsorbed superoxide (OOH_{ad}) (Figure S28, Supporting Information). This profile indicates that an adsorbate evolution mechanism rather than a lattice oxygen evolution mechanism (straightforward insertion/removal of oxygen in and out of the lattice) dominated O_2 generation over the $\text{Re}_{0.1}\text{-IrO}_2$ electrode, which contributed to an improved stability of the electrocatalysts under acidic conditions.^[46] These results confirm the high OER activity and stability of the $\text{Re}_{0.1}\text{-IrO}_2$ electrode, and validate that multiple valence state of the Re atoms could adjust the unique structure arrangement of IrO_2 and minimize the dissolution of Ir.

3. Conclusion

In summary, the authors rationally designed and synthesized Re-doped IrO_2 with low crystallinity as highly efficient and robust electrocatalysts for the acidic OER. DFT calculations suggest that incorporation of Re into IrO_2 contributes to the spontaneous substitution energy and high sintering resistance. The optimized $\text{Re}_{0.1}\text{-IrO}_2$ catalyst exhibited a current density of 10 mA cm^{-2} , only requiring a low overpotential of 255 mV in acidic media. Extensive experiments and theoretical analyses demonstrated that the robust durability and improved activity of $\text{Re}_{0.1}\text{-IrO}_2$ were mainly attributed to the pivotal roles of the Re dopants for modulating the electronic structure of IrO_2 . The facilitated $^*\text{OH}$ adsorption and $^*\text{OOH}$ deprotonation resulted in improved catalytic kinetics of $\text{Re}_{0.1}\text{-IrO}_2$ during the OER. In situ Raman and ex situ XPS measurements indicated suppressed over-oxidation of the Ir in $\text{Re}_{0.1}\text{-IrO}_2$ in the presence of Re dopants, which minimized the dissolution of Ir and enhanced the catalytic stability for the acidic OER. This study will facilitate the design and development of high-performance electrocatalysts for energy conversion.

Supporting Information

Supporting Information is available from the Wiley Online Library or from the author.

Acknowledgements

This work was supported in part by the National Natural Science Foundation of China (Grant Nos. 22109119, 51972238, and 21875166) and the Basic Scientific Research Projects of Wenzhou City (H20210006).

Conflict of Interest

The authors declare no conflict of interest.

Data Availability Statement

The data that support the findings of this study are available from the corresponding author upon reasonable request.

Keywords

chemical doping, iridium (IV) oxide, low crystallization, oxygen evolution reaction, rhenium

Received: December 15, 2022

Revised: January 25, 2023

Published online:

[1] J. Song, C. Wei, Z.-F. Huang, C. Liu, L. Zeng, X. Wang, Z. J. Xu, *Chem. Soc. Rev.* **2020**, *49*, 2196.

[2] Y. Jiao, Y. Zheng, M. T. Jaroniec, S. Z. Qiao, *Chem. Soc. Rev.* **2015**, *44*, 2060.

- [3] S. Shen, Z. Hu, H. Zhang, K. Song, Z. Wang, Z. Lin, Q. Zhang, L. Gu, W. Zhong, *Angew. Chem., Int. Ed.* **2022**, *134*, e202206460.
- [4] Z. Lin, B. Xiao, M. Huang, L. Yan, Z. Wang, Y. Huang, S. Shen, Q. Zhang, L. Gu, W. Zhong, *Adv. Energy Mater.* **2022**, *12*, 2200855.
- [5] S. Ma, J. Deng, Y. Xu, W. Tao, X. Wang, Z. Lin, Q. Zhang, L. Gu, W. Zhong, *J. Energy Chem.* **2022**, *66*, 560.
- [6] L. C. Seitz, C. F. Dickens, K. Nishio, Y. Hikita, J. Montoya, A. Doyle, C. Kirk, A. Vojvodic, H. Y. Hwang, J. K. Nørskov, T. F. Jaramillo, *Science* **2016**, *353*, 1011.
- [7] W. Song, M. Li, C. Wang, X. Lu, *Carbon Energy* **2021**, *3*, 101.
- [8] C. C. L. McCrory, S. Jung, I. M. Ferrer, S. M. Chatman, J. C. Peters, T. F. Jaramillo, *J. Am. Chem. Soc.* **2015**, *137*, 4347.
- [9] Y. Jin, W. Huo, L. Zhang, Y. Li, Q. Chen, X. Zhang, S. Yang, H. Nie, X. Zhou, Z. Yang, *Chem. Commun.* **2021**, *57*, 7168.
- [10] Z. Chen, X. Duan, W. Wei, S. Wang, B.-J. Ni, *Nano Energy* **2020**, *78*, 105392.
- [11] Y. Zhao, M. Luo, S. Chu, M. Peng, B. Liu, Q. Wu, P. Liu, F. M. F. de Groot, Y. Tan, *Nano Energy* **2019**, *59*, 146.
- [12] R. Li, H. Wang, F. Hu, K. C. Chan, X. Liu, Z. Lu, J. Wang, Z. Li, L. Zeng, Y. Li, X. Wu, Y. Xiong, *Nat. Commun.* **2021**, *12*, 3540.
- [13] Z. Chen, X. Duan, W. Wei, S. Wang, B.-J. Ni, *Nano Energy* **2020**, *78*, 105270.
- [14] W. Gou, Z. Xia, X. Tan, Q. Xue, F. Ye, S. Dai, M. Zhang, R. Si, Y. Zou, Y. Ma, J. C. Ho, Y. Qu, *Nano Energy* **2022**, *104*, 107960.
- [15] M. Elmaalouf, M. Odziomek, S. Duran, M. Gayraud, M. Bahri, C. Tard, A. Zitolo, B. Lassalle-Kaiser, J.-Y. Piquemal, O. Ersen, C. Boissière, C. Sanchez, M. Giraud, M. Faustini, J. Peron, *Nat. Commun.* **2021**, *12*, 3935.
- [16] A. Grimaud, A. Demortière, M. Saubanière, W. Dachraoui, M. Duchamp, M.-L. Doublet, J.-M. Tarascon, *Nat. Energy* **2016**, *2*, 16189.
- [17] L. She, G. Zhao, T. Ma, J. Chen, W. Sun, H. Pan, *Adv. Funct. Mater.* **2022**, *32*, 2108465.
- [18] L. An, C. Wei, M. Lu, H. Liu, Y. Chen, G. G. Scherer, A. C. Fisher, P. Xi, Z. J. Xu, C.-H. Yan, *Adv. Mater.* **2021**, *33*, 2006328.
- [19] Y. Chen, J. Cai, P. Li, G. Zhao, G. Wang, Y. Jiang, J. Chen, S. X. Dou, H. Pan, W. Sun, *Nano Lett.* **2020**, *20*, 6807.
- [20] E. Oakton, D. Lebedev, M. Povia, D. F. Abbott, E. Fabbri, A. Fedorov, M. Nachttegaal, C. Copéret, T. J. Schmidt, *ACS Catal.* **2017**, *7*, 2346.
- [21] Z. Cheng, Y. Pi, Q. Shao, X. Huang, *Sci. China Mater.* **2021**, *64*, 2958.
- [22] T. Kwon, M. Jun, G. J. Bang, H. Yang, J. Joo, T. Kim, J. Kim, J. M. Kim, H. Baik, Y. Jung, J. Y. Kim, K. Lee, *Cell Rep. Phys. Sci.* **2020**, *1*, 100260.
- [23] Y. Jin, W. Huo, X. Zhou, L. Zhang, Y. Li, S. Yang, J. Qian, D. Cai, Y. Ge, Z. Yang, H. Nie, *Chem. Commun.* **2023**, *59*, 183.
- [24] F. Lv, J. Feng, K. Wang, Z. Dou, W. Zhang, J. Zhou, C. Yang, M. Luo, Y. Yang, Y. Li, P. Gao, S. Guo, *ACS Cent. Sci.* **2018**, *4*, 1244.
- [25] G.-Y. Kim, J. Lee, Y.-J. Rho, W.-H. Kim, M. Kim, J.-H. Ahn, W.-H. Ryu, *Chem. Eng. J.* **2022**, *446*, 136951.
- [26] A. Vargas-Uscategui, E. Mosquera, B. Chornik, L. Cifuentes, *Electrochim. Acta* **2015**, *178*, 739.
- [27] Y. L. Kim, H.-A. Choi, N.-S. Lee, B. Son, H. J. Kim, J. M. Baik, Y. Lee, C. Lee, M. H. Kim, *Phys. Chem. Chem. Phys.* **2015**, *17*, 7435.
- [28] Y. Ha, Y. Lee, A. Yu, S. H. Lee, C. Lee, M. H. Kim, Y. Lee, *Curr. Appl. Phys.* **2021**, *21*, 20.
- [29] M. Huang, J. Zhu, *Rare Met.* **2016**, *35*, 127.
- [30] J. Purans, A. Kuzmin, E. Cazzanelli, G. Mariotto, *J. Phys.: Condens. Matter* **2007**, *19*, 226206.
- [31] V. Pfeifer, T. E. Jones, J. J. Velasco Vélez, C. Massué, R. Arrigo, D. Teschner, F. Girgsdies, M. Scherzer, M. T. Greiner, J. Allan, M. Hashagen, G. Weinberg, S. Piccinin, M. Hävecker, A. Knop-Gericke, R. Schlögl, *Surf. Interface Anal.* **2016**, *48*, 261.
- [32] J. Gao, C.-Q. Xu, S.-F. Hung, W. Liu, W. Cai, Z. Zeng, C. Jia, H. M. Chen, H. Xiao, J. Li, Y. Huang, B. Liu, *J. Am. Chem. Soc.* **2019**, *141*, 3014.
- [33] X. Zhou, Z. Tian, J. Li, H. Ruan, Y. Ma, Z. Yang, Y. Qu, *Nanoscale* **2014**, *6*, 2603.
- [34] J. He, X. Zhou, P. Xu, J. Sun, *Adv. Energy Mater.* **2021**, *11*, 2102883.
- [35] Z. Xiao, Y.-C. Huang, C.-L. Dong, C. Xie, Z. Liu, S. Du, W. Chen, D. Yan, L. Tao, Z. Shu, G. Zhang, H. Duan, Y. Wang, Y. Zou, R. Chen, S. Wang, *J. Am. Chem. Soc.* **2020**, *142*, 12087.
- [36] W. Chen, B. Wu, Y. Wang, W. Zhou, Y. Li, T. Liu, C. Xie, L. Xu, S. Du, M. Song, D. Wang, Y. Liu, Y. Li, J. Liu, Y. Zou, R. Chen, C. Chen, J. Zheng, Y. Li, J. Chen, S. Wang, *Energy Environ. Sci.* **2021**, *14*, 6428.
- [37] W. Gou, M. Zhang, Y. Zou, X. Zhou, Y. Qu, *ChemCatChem* **2019**, *11*, 6008.
- [38] J. Xu, Z. Lian, B. Wei, Y. Li, O. Bondarchuk, N. Zhang, Z. Yu, A. Araujo, I. Amorim, Z. Wang, B. Li, L. Liu, *ACS Catal.* **2020**, *10*, 3571.
- [39] T. Zhao, X. Shen, Y. Wang, R. K. Hocking, Y. Li, C. Rong, K. Dastafkan, Z. Su, C. Zhao, *Adv. Funct. Mater.* **2021**, *31*, 2100614.
- [40] W. Sun, Y. Song, X.-Q. Gong, L.-m. Cao, J. Yang, *Chem. Sci.* **2015**, *6*, 4993.
- [41] J. Huang, H. Sheng, R. D. Ross, J. Han, X. Wang, B. Song, S. Jin, *Nat. Commun.* **2021**, *12*, 3036.
- [42] M. Wang, C.-L. Dong, Y.-C. Huang, Y. Li, S. Shen, *Small* **2018**, *14*, 1801756.
- [43] C.-L. Ma, X.-R. Yang, Z.-Q. Wang, W. Sun, L. Zhu, L.-M. Cao, X.-Q. Gong, J. Yang, *ACS Appl. Mater. Interfaces* **2022**, *14*, 28706.
- [44] S. Geiger, O. Kasian, M. Ledendecker, E. Pizzutilo, A. M. Mingers, W. T. Fu, O. Diaz-Morales, Z. Li, T. Oellers, L. Fruchter, A. Ludwig, K. J. J. Mayrhofer, M. T. M. Koper, S. Cherevko, *Nat. Catal.* **2018**, *1*, 508.
- [45] Z. Pavlovic, C. Ranjan, Q. Gao, M. van Gastel, R. Schlögl, *ACS Catal.* **2016**, *6*, 8098.
- [46] R. Nakamura, A. Imanishi, K. Murakoshi, Y. Nakato, *J. Am. Chem. Soc.* **2003**, *125*, 7443.